F-region electron density and Te / Ti measurements using incoherent scatter power data collected at ALTAIR

M. Milla, E. Kudeki

Ann. Geophys., 24, 1333–1342, 2006
www.ann-geophys.net/24/1333/2006/

Annales Geophysicae

F-region electron density and T_e/T_i measurements using incoherent scatter power data collected at ALTAIR

M. Milla and E. Kudeki

Department of Electrical and Computer Engineering, University of Illinois at Urbana-Champaign, Illinois, USA

Received: 23 November 2005 – Revised: 10 February 2006 – Accepted: 14 February 2006 – Published: 3 July 2006

Part of Special Issue "The 11th International Symposium on Equatorial Aeronomy (ISEA-11), Taipei, May 2005"

Abstract. The ALTAIR UHF radar was used in an incoherent scatter experiment to observe the low-latitude ionosphere during the Equis 2 rocket campaign. The measurements provided the first high-resolution electron density maps of the low-latitude D- and E-region in the Pacific sector and also extended into the F-region and topside ionosphere. Although the sampling frequency was well below the Nyquist frequency of F-region returns, we were able to estimate T_e/T_i ratio and infer unbiased electron density estimates using a regularized inversion technique described here. The technique exploits magnetic aspect angle dependence of ISR cross-section for $T_e > T_i$.

Keywords. Ionosphere (Equatorial ionosphere; Plasma temperature and density) – Radio science (Remote sensing)

1 Introduction

During the 2004 Equis 2 NASA Rocket Campaign, incoherent scatter radar (ISR) measurements of the low-latitude daytime ionosphere were conducted using the ALTAIR UHF radar. The measurements were made for common volume comparisons with rocket based D- and E-region electron density estimates described in Friedrich et al. (2006). During the observations, ALTAIR beam was scanned along a north-south oriented plane that coincides with the rocket trajectory, and ISR signal returns were sampled from D-region up to the topside F-region heights. The scan geometry and radar data collected in a single scan (lasting about 5 min 20 s) are illustrated in Fig. 1 where the color map corresponds to the logarithm of backscattered power. A detailed analysis of the power data shown in this figure and how it can be used to obtain F-region density maps corrected for T_e/T_i variations throughout the bottom-side F-region are the main concerns of this paper.

As the ALTAIR beam was scanned, it probed the ionosphere at different magnetic aspect angles, going through a perpendicular orientation with respect to the geomagnetic field at an elevation of $\sim 80°$. That orientation coincides with the spike-like intrusion seen in Fig. 1. This is better illustrated in Fig. 2 where power is now displayed as function of elevation angle and height. The superposed white arrows depict the relative orientation of the geomagnetic field $\boldsymbol{B}$ with respect to the radar beam direction over a sample grid. The enhanced power corresponding to the spike observed in both figures is characteristic of incoherent scatter (IS) process for probing directions perpendicular to $\boldsymbol{B}$ and for heights where electron temperature exceeds the ion temperature (i.e., $T_e > T_i$). The theory presented by Farley (1966) quantifies this enhancement in terms of IS radar cross-section (RCS) that depends on electron density N_e, T_e/T_i ratio, and magnetic aspect angle α. The RCS function constitutes the core of a forward model for the power data displayed in Fig. 1 which will be used to infer the height distributions of N_e and T_e/T_i as described in Sect. 4.

In practice, the standard RCS function of Farley (1966) is inaccurate – and, in fact, unspecified – for small aspect angles α where electron and ion Coulomb collisions are becoming important as shown by Sulzer and González (1999). Since the ALTAIR beam goes through $\alpha = 0°$, we had to extend the RCS model to include these collisional effects. This was done by using the collisional incoherent scatter spectrum model described by Woodman (1967) and Kudeki et al. (1999), and an empirical collision frequency model proposed by Woodman (2004).

Another detail of the measurements concerns the linear frequency modulation (LFM) used to generate the transmitted radar pulses. The response of the resultant "chirped" pulse was modeled in terms of the corresponding radar ambiguity function (AF) and its influence on the collected power

Correspondence to: E. Kudeki
(erhan@uiuc.edu)

Published by Copernicus GmbH on behalf of the European Geosciences Union.

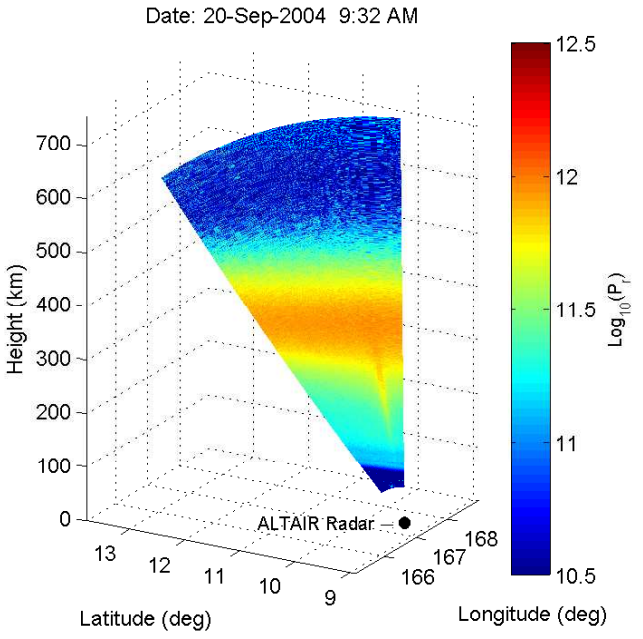

Fig. 1. An example of the ALTAIR scan measurements collected during the Equis 2 campaign. In colors, levels of backscattered power calibrated to match electron densities in the probed region are displayed.

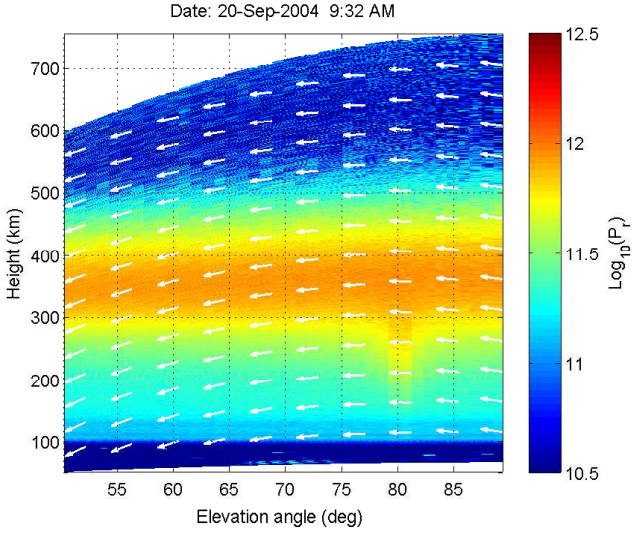

Fig. 2. Backscattered power data displayed as function of beam elevation angle and height. The white arrows depict the relative orientation of the geomagnetic field with respect to the radar beam direction over a sample grid. Note that the power enhancement at $\sim 80°$ elevation is from altitudes with $T_e > T_i$ and a radar line-of-sight perpendicular to $\boldsymbol{B}$.

Table 1. Experiment configuration.

Radar parameters	
Peak power	4 MW
Radar frequency	422 MHz
Pulse modulation	250 kHz LFM
Pulse width	400 µsec (60 km)
Inter-pulse period	8.3 msec (1250 km)
Sampling rate	1.6 µsec (240 m)
Range	65 − 755 km

data was included in the forward model used to estimate N_e and T_e/T_i.

The paper is organized as follows: after a brief description of the radar configuration in Sect. 2, we present, in Sect. 3, the derivation of the forward theory model for backscattered ISR power, including the AF analysis of transmitted pulses and our extended ISR RCS model, as outlined above. Section 4 describes our inversion method to estimate the N_e and T_e/T_i profiles from measured power data, namely, a regularized least-squares minimization algorithm relying on a graphic criterion for optimal selection of the regularization parameter (L-curve). Finally, Sect. 6 is devoted to the presentation of our results, N_e and T_e/T_i, and their discussion.

2 Radar measurements

ALTAIR, located on Roi-Namur island (9.39° N, 167.47° E) of the Kwajalein Atoll, is a dual-band (VHF and UHF) high-sensitivity radar designed for missile detection and tracking. Its 150-ft parabolic dish antenna is fully steerable with angular rates of up to 10°/s (Lemnios and Grometstein, 2002). Its transmitter can deliver up to 4 MW of peak power in the UHF band with a maximum duty cycle of 5%. In transmission, circularly polarized pulses are used while in reception both right- and left-circularly polarized returns are monitored and detected independently.

Table 1 presents a summary of the primary ALTAIR parameters used in ionospheric measurements conducted on 20 September 2004. As indicated, the radar was operated using a LFM waveform (chirped pulse) of 400 µs duration, 422 MHz center frequency, 250 kHz bandwidth, and a 120 Hz pulse repetition frequency (PRF) corresponding to a 8.33 ms inter-pulse period (IPP) greater than the correlation time of ISR signal returns. The pulse compression effect which results upon a matched filter detection of the pulse returns will be described and formulated in the next section. The matched-filter receiver outputs were sampled at a rate corresponding to 240 m radar range, and 2874 gates were sampled to cover from 65 to 755 km of radar range. During each scan the radar beam was swept in the −13.5° azimuth

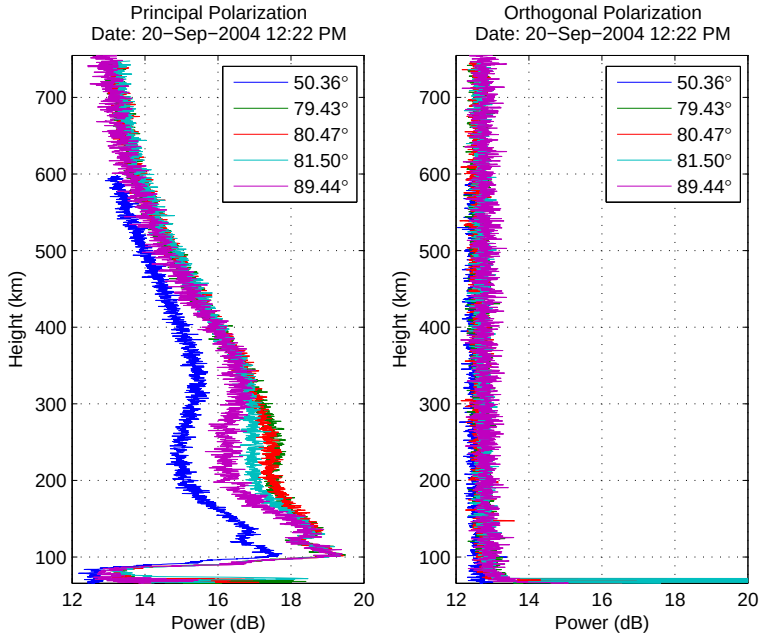

Fig. 3. Power profiles measured with both circularly polarized antenna channels at different elevation angles. Note that depolarization of the return signal was not detected given that generalized Faraday effects are negligible at 422 MHz.

plane from an elevation angle of 50° to zenith position in about 5 min and 20 s (at 8 s/deg rate).

In Fig. 3, we display power versus height calculated from matched-filter receiver outputs of the right- and left-circularly polarized antenna channels. The individual profiles in Fig. 3 correspond to different elevation angles of the ALTAIR beam and represent an integration over 1000 radar pulses (i.e., 8.33 s) during which the beam moves about 1°. Notice that only the channel labeled as "principal polarization" contains backscattered radar power, indicating that possible depolarization effects can be neglected in our analysis. This is an expected result, not only because circularly polarized transmissions correspond to a normal mode of propagation for most scanning directions involved, but also because generalized Faraday effects (e.g. Yeh et al., 1999) are very weak at 422 MHz even for propagation perpendicular to the geomagnetic field (in which case the normal modes are linearly polarized).

In the next section we develop a quantitative model for the enhanced power data recorded in the principal polarization channel, which is subsequently used in Sect. 4 to estimate N_e and T_e/T_i profiles in the probed regions.

3 Data model and radar calibration

3.1 Radar equation and ambiguity function (AF)

In soft-target Bragg scattering each infinitesimal volume $dv \equiv r^2 dr d\Omega$ of a radar field-of-view behaves like a hard-target with a radar cross-section (RCS) $dv \int \frac{d\omega}{2\pi} \sigma(\boldsymbol{k}, \omega)$, where $\sigma(\boldsymbol{k}, \omega)$, by definition, is soft-target RCS per unit volume per unit Doppler frequency $\frac{\omega}{2\pi}$, and $\boldsymbol{k} \equiv -2k_o\hat{r}$ denotes the relevant Bragg vector for a radar with a carrier wavenumber k_o. As a consequence, hard-target radar equation generalizes for soft-target Bragg-scatter radars as

$$P_r(t) = \int dr d\Omega \frac{d\omega}{2\pi} \frac{G(\hat{r})A(\hat{r})}{(4\pi r)^2} P_t \left(t - \frac{2r}{c}\right) \sigma(\boldsymbol{k}, \omega), \quad (1)$$

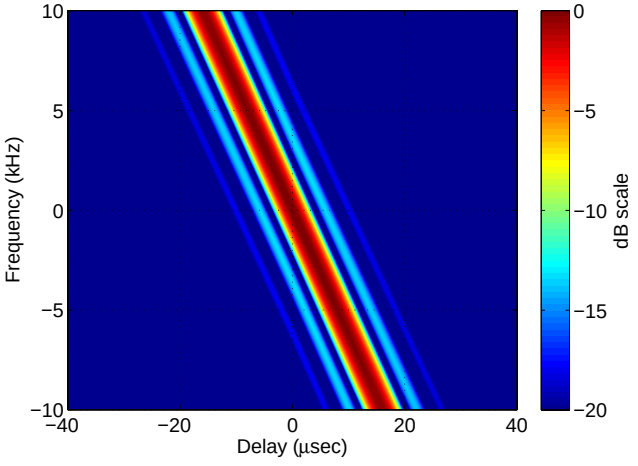

Fig. 4. Ambiguity function $|\chi(\tau, \omega)|$ of a chirp pulse of width T=400 μsec and frequency span Δf=250 kHz.

where $P_t(t) \propto |f(t)|^2$ is the transmitted power carried by a pulse waveform $f(t)$, $G(\hat{r})$ and $A(\hat{r})$ are the gain and effective area of the radar antenna as a function of radial unit vector $\hat{r}$, r is the radar range, and c the speed of light. Furthermore, Eq. (1), which assumes an open radar bandwidth, can be re-cast for a match-filtered receiver output as

$$\frac{P_r(t)}{E_t K_s} = \int dr d\Omega \frac{d\omega}{2\pi} \frac{g^2(\hat{r})}{r^2} |\chi\left(t - \frac{2r}{c}, \omega\right)|^2 \sigma(\boldsymbol{k}, \omega), \quad (2)$$

where E_t is the total energy of the transmitted radar pulse, K_s denotes a system calibration constant including loss factors ignored in Eq. (1), $g(\hat{r})$ is the self-normalized version of $G(\hat{r})$, and

$$\chi(\tau, \omega) \equiv \frac{1}{T} \int dt\ e^{j\omega t}\ f(t) f^*(t - \tau) \quad (3)$$

has a magnitude known as radar *ambiguity function* (e.g., Levanon, 1988). In Eq. (3) the normalization constant T denotes the duration of pulse waveform $f(t)$ and Eq. (3) itself is effectively the normalized cross-correlation of Doppler-shifted pulse $f(t)e^{j\omega t}$ with a delayed pulse echo $\propto f(t-\tau)$ that would be expected from a point target located at a radar range $c\tau/2$. Hence, variable τ in Eq. (3) not only represents a time delay, but also a corresponding radar range r, and we will refer to τ as delay or range as we find convenient in the following discussion.

In our experiment, we used a chirped pulse waveform

$$f(t) = \text{rect}(t/T) e^{j\frac{\beta}{2}t^2}, \quad (4)$$

which, in effect, causes a slow linear variation of the carrier frequency over a bandwidth Δf and at a rate $\frac{\beta}{2\pi} = \frac{\Delta f}{T}$. The corresponding ambiguity function,

$$|\chi(\tau, \omega)| = \triangle\left(\frac{\tau}{2T}\right) |\text{sinc}\left(\frac{(T - |\tau|)(\omega + \beta\tau)}{2}\right)|, \quad (5)$$

is plotted in Fig. 4 for T=400 µs and Δf=250 kHz (parameters used in the experiment).

According to Eq. (5), the overall width of $|\chi(\tau, \omega)|$ along the delay axis τ over the frequency bandwidth B of the RCS spectrum corresponds to $2\pi B/\beta$ (given $B \ll \Delta f$), which implies a range resolution Δr – defined as the range separation between independent measurements – described by

$$\frac{2\Delta r}{c} = \frac{2\pi B}{\beta} = \frac{TB}{\Delta f}. \quad (6)$$

For instance, for a plausible ionospheric bandwidth of B=10 kHz, the range resolution is Δr=2.4 km. In addition, any mean Doppler shift of the RCS spectrum will imply a displacement of the actual position of the backscatter signal; such a displacement can be estimated as

$$d = f_o T \frac{v_d}{\Delta f}, \quad (7)$$

where v_d is the Doppler shift measured in m/s and f_o the radar carrier frequency in Hz. In ionospheric observations, possible Doppler shifts are around 100 m/s, with a corresponding displacement of about 67 m, a small fraction of the range resolution Δr that can be safely neglected.

Assuming that $\sigma(\boldsymbol{k}, \omega)$ varies slowly with the radar range r, and that the AF is almost flat within the bandwidth of the RCS spectrum (which is the case of this application), we can simplify Eq. (2) to obtain

$$\frac{P_r(R)}{E_t K_s} \approx \frac{\delta R}{R^2} \int d\Omega g^2(\hat{r}) \sigma_T(\boldsymbol{k}), \quad (8)$$

where $R = \frac{ct}{2}$ is the measured radar range,

$$\delta R \equiv \int dr |\chi\left(\frac{2}{c}(R - r), 0\right)|^2 \quad (9)$$

is the effective range depth of the radar scattering volume, and

$$\sigma_T(\boldsymbol{k}) \equiv \int \frac{d\omega}{2\pi} \sigma(\boldsymbol{k}, \omega) \quad (10)$$

is the total volumetric RCS where dependence on range R is implied.

3.2 Incoherent scatter RCS spectrum (σ)

The IS theory establishes that the volumetric RCS spectrum of a quiescent ionosphere can be written as (e.g. Dougherty and Farley, 1960; Farley et al., 1961)

$$\sigma(\boldsymbol{k}, \omega) = 4\pi r_e^2 \langle |n_e(\boldsymbol{k}, \omega)|^2 \rangle \quad (11)$$

where r_e is the classical electron radius and

$$\langle |n_e(\boldsymbol{k}, \omega)|^2 \rangle = \frac{2N_e}{\omega} \left\{ \frac{|jk^2\lambda_e^2 + \mu y_i(\boldsymbol{k}, \omega)|^2 \text{Re}\{y_e(\boldsymbol{k}, \omega)\}}{|jk^2\lambda_e^2 + y_e(\boldsymbol{k}, \omega) + \mu y_i(\boldsymbol{k}, \omega)|^2} + \frac{|y_e(\boldsymbol{k}, \omega)|^2 \text{Re}\{y_i(\boldsymbol{k}, \omega)\}}{|jk^2\lambda_e^2 + y_e(\boldsymbol{k}, \omega) + \mu y_i(\boldsymbol{k}, \omega)|^2} \right\} \quad (12)$$

denotes the space-time spectrum of electron density fluctuations. Above, N_e is the mean electron density, λ_e is the electron Debye length, μ the temperature ratio T_e/T_i, and y_e and y_i are normalized electron and ion admittance functions proportional to conductivities in the medium. These admittances can be expressed as

$$y_s = j + \theta_s J_s(\theta_s), \quad (13)$$

where s denotes each species (electrons or ions) and $\theta_s \equiv \frac{\omega}{\sqrt{2}kC_s}$ is the frequency normalized by wavenumber k and thermal speed C_s. The function J_s, that will be specified later, is a Gordeyev integral that can be interpreted as one-sided Fourier transform of normalized auto-correlation of echoes from charged particles in the absence of collective interactions (e.g. Hagfors and Brockelman, 1971).

Replacing Eq. (11) in Eq. (8), we have

$$\frac{P_r(R)}{E_t K_s} \approx \frac{4\pi r_e^2 N_e(R) \delta R}{R^2} \int d\Omega g^2(\hat{r}) \eta(\boldsymbol{k}), \quad (14)$$

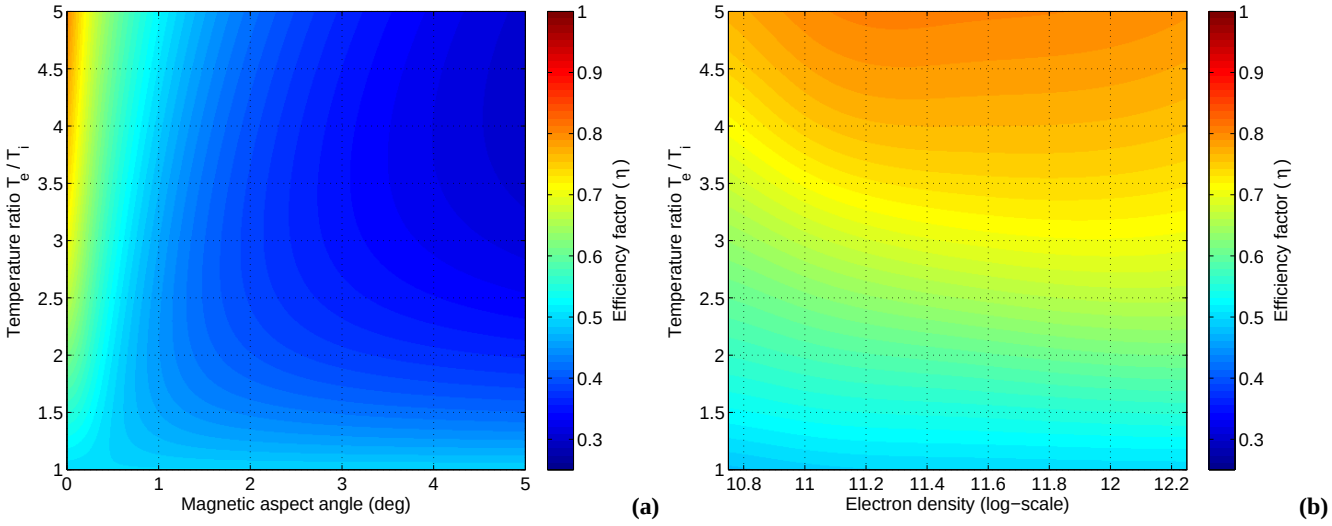

Fig. 5. Efficiency factor η as function of **(a)** magnetic aspect angle vs. T_e/T_i for a constant electron density of $10^{12}\,\mathrm{m}^{-3}$, and **(b)** electron density vs. T_e/T_i at perpendicular to $\boldsymbol{B}$. Both graphics correspond to the case of T_e=1000 K.

where

$$\eta(\boldsymbol{k}) \equiv \int \frac{d\omega}{2\pi} \frac{\langle |n_e(\boldsymbol{k},\omega)|^2 \rangle}{N_e} \tag{15}$$

is an efficiency factor that is $\frac{1}{2}$ in a plasma in thermodynamic equilibrium, or, more generally, $(1+\frac{T_e}{T_i})^{-1}$ in a non-magnetized plasma with an arbitrary T_e/T_i and negligible Debye length (e.g. Farley, 1966). But, in our forward model, we will need the efficiency η for a magnetized plasma with an arbitrary T_e/T_i and for arbitrarily small aspect angles. Here, we define the aspect angle α as the complement of the angle between probing vector $\boldsymbol{k}$ and geomagnetic field $\boldsymbol{B}$.

In general, non-collisional models for (12) become singular as $\alpha \to 0°$ and make numerical evaluation of η impossible in the same limit. This difficulty can be circumvented by using a collisional model for Eq. (12). In our computations of η, we used the collisional model developed by Woodman (1967), which is based on a simplified Fokker-Planck operator for Coulomb collisions, the relevant collision process for F-region altitudes (e.g. Sulzer and González, 1999). The model leads to a Gordeyev integral (e.g. Kudeki et al., 1999; Kudeki and Milla, 2006)

$$J_s(\theta_s) = \int_0^\infty dt e^{-j\theta_s t} e^{-\frac{\psi_s t - 1 + e^{-\psi_s t}}{2\psi_s^2} \sin^2\alpha} e^{-\frac{\cos(2\gamma_s) + \psi_s t - e^{-\psi_s t}\cos(\phi_s t - 2\gamma_s)}{2(\psi_s^2+\phi_s^2)} \cos^2\alpha}, \tag{16}$$

where $\psi_s \equiv \frac{\nu_s}{\sqrt{2}kC_s}$ and $\phi_s \equiv \frac{\Omega_s}{\sqrt{2}kC_s}$ are normalized collision- and gyro-frequencies, respectively, and $\gamma_s \equiv \tan^{-1}(\frac{\nu_s}{\Omega_s})$. For ν_i and ν_e we make use of the collision frequency models of Woodman (1967) and Woodman (2004), respectively, which are

$$\nu_i/\nu_{i0} = 0.601 \tag{17}$$

and (Eq. (14) in the original paper)

$$\nu_e/\nu_{e0} = 1.06 + 7.55\sin\alpha/\sin\alpha_c - 2.00(\sin\alpha/\sin\alpha_c)^2 + 0.27(\sin\alpha/\sin\alpha_c)^3, \tag{18}$$

where $\alpha_c \equiv \sin^{-1}(\frac{2\pi\nu_{e0}}{kC_e})$ is a critical aspect angle and

$$\nu_{s0} \equiv \frac{e^4 N_e}{4\pi\epsilon_0^2 m_s^{1/2}(2KT_s)^{3/2}} \ln(24\pi\lambda_e^3 N_e) \tag{19}$$

is the so-called Spitzer collision frequency for species s (electrons or ions).

In numerical evaluations of η, Gordeyev integrals J_s were computed using a chirp z-transform algorithm suggested by Li et al. (1991). Each integral was evaluated for a total of 2^{15} sample frequencies equally spaced from 0 to 125 kHz. The algorithm samples the integrand of J_s in sections of the same length, and adds iteratively the contribution of each section as it is needed for convergence of the integral. Despite the accuracy that this algorithm provides, it became computationally demanding to obtain J_s at angles close to perpendicular to $\boldsymbol{B}$ because of the narrowness of the IS spectrum in this regime. Nevertheless, computations were possible even at α=0° as a consequence of the collisional model used.

We have calculated the efficiency factor η for different values of aspect angle α, temperature ratio T_e/T_i, and electron density N_e. As an example, we display in Fig. 5a the values of η computed for a constant density of $10^{12}\,\mathrm{m}^{-3}$ and T_e=1000 K. Here, we can notice that the dependence of η

on the magnetic aspect angle becomes relevant for small α (smaller than $\sim 3°$). In addition, Fig. 5b shows the variation of the efficiency factor as function of N_e for $\alpha = 0°$ and $T_e = 1000$ K. In this case, η increases as T_e/T_i rises from unity. Note that the rate of change is not uniform for different density values.

Overall, we have found that η is not highly sensitive to variations of the collision frequency parameter. For instance, increasing ν_e by factor of 3 or decreasing it by a factor of 10 did not change the computed η values by more than $\sim 1\%$. On the other hand, drastic changes, such as a factor of 30 increase in ν_e, cause noticeable changes in η.

3.3 Radar calibration and backscattered power calculations

The use of Eq. (14) to model the measured power data requires the availability of transmitted pulse energy E_t and system constant K_s. Since the transmitted peak power P_t is recorded in ALTAIR data headers on a per pulse basis, the pulse energy is trivially obtained as $E_t \equiv P_t T$. In addition, the K_s value that accounts for all the losses and gains of the entire system is available from power measurements conducted with a hard target of a known RCS. The effective range depth δR needed in Eq. (14) is obtained by using Eq. (9) with radar returns detected from a suitable point target.

The computation of the solid angle integral in Eq. (14) was simplified assuming that ionospheric parameters do not vary locally in longitude, therefore, only changes along the direction of the scan were considered. This assumption is justified by the narrowness of the ALTAIR UHF antenna beam with a beam-width of less than one degree. As a result, we collapsed the solid integral into a 1-D angular integral along the direction of the scan. Moreover, because only a few points of the antenna pattern were available from calibration measurements, we used a Fourier interpolation method to improve the angular grid of the normalized antenna gain.

We considered two different approaches to evaluate the angular integral just described: The first one corresponds to assuming a fixed beam direction during the transmission of the 1000 pulses used to obtain a single averaged power profile. This approach is justified if the efficiency factor η varies linearly across the beam, in which case, it can be replaced by its central value and reduce the integral to the calculation of an equivalent solid angle. In the second approach, we accounted for the effect of the angular displacement of the beam from pulse to pulse and averaged the 1000 profiles corresponding to each beam position to obtain a model profile for the measured power data. Comparison of the two methods revealed negligible differences in test cases, and, as a consequence, the bulk of the results to be presented in the next section were obtained using the less costly first approach.

4 Inversion technique

A regularized least-squares fitting algorithm (e.g. Tikhonov and Arsenin, 1977) was used to perform electron density and T_e/T_i estimations from the modeled power data. In general, a regularization technique allows us to introduce some prior information about the characteristics of the parameters to be estimated in order to obtain better results. Next, we will describe our algorithm and the assumptions we made in this work.

First, we envisioned the ionosphere as a stratified medium composed of layers of a fixed width that extend along longitude and latitude following the curvature of the Earth, such that, in each layer, the density and temperature ratio can be considered constants. Below, the vectors $\boldsymbol{N}_e$ and $\boldsymbol{T}_r$ denote respectively the electron density and T_e/T_i profiles that were estimated after minimizing the following cost function

$$\underbrace{\sum_i \left(\frac{p_m^i - P_r^i(\boldsymbol{N}_e, \boldsymbol{T}_r)}{\sigma_p^i} \right)^2}_{\text{Data-term}} + \underbrace{\lambda^2 \sum_j (T_r^{j+1} - T_r^j)^2}_{\text{Regularization-term}} . \quad (20)$$

In this expression, p_m is the measured power collected by the radar, and P_r and σ_p denote its model and standard deviation. Our power model also accounts for the noise level detected by the radar receiver, level that was estimated from samples taken below 80 km altitude. Above, the variable λ denotes the regularization parameter, and its significance will be discussed later in this section.

In Eq. (20), the index i implies summation over a set of radar ranges and scanning angles that correspond to the region where the power enhancement was observed. Thus, we are considering seven data profiles whose magnetic aspect angles are between $-2.5°$ and $2.5°$ (and corresponding scanning directions between $77°$ and $83°$). In range, samples taken at each 6 km (which is also the width of each j-th layer) provide a good enough resolution to characterize the F-region.

The simple form of the data-term in Eq. (20) is justified by the independence of our measurements. Based on our AF analysis, we know that samples with a separation of 6 km are range independent. In addition, given that the inter-pulse period of the experiment (8.33 ms) was longer than the correlation time of ISR returns, there is no angular or pulse-to-pulse correlation between power profiles. Therefore, we can define the standard deviation of the measured power as $\sigma_p \equiv \frac{p_m}{\sqrt{n_i}}$, n_i being the number of incoherent integrations (averages) performed to obtain an individual profile. Here, it is useful to indicate that at 422 MHz, the correlation time of beam weighted ISR returns coming from the region around perpendicular to $\boldsymbol{B}$ is of the order of 1 ms.

From the analysis of our power model, it turns out that the dependence of the measurements on the plasma density is stronger than its dependence on T_e/T_i. Therefore, at ranges

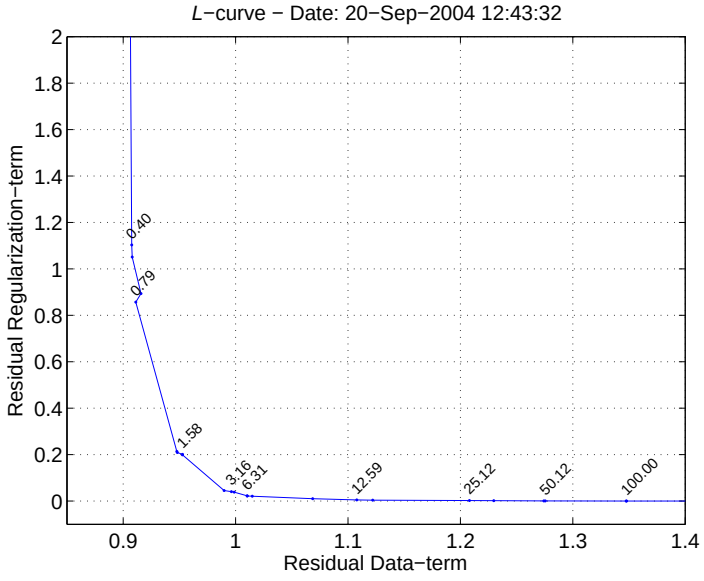

Fig. 6. An example of the *L*-curves we computed for optimal selection of the regularization parameter. Note that the corner of the curve represents a trade-off between the residuals of the data- and regularization-terms.

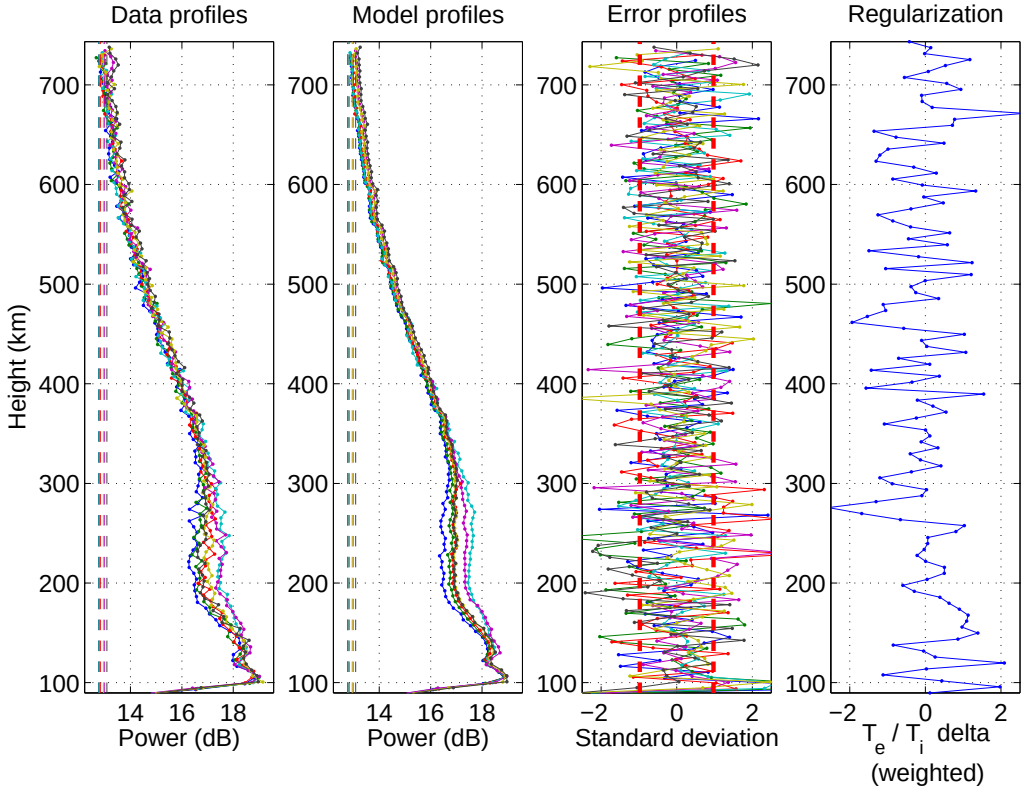

Fig. 7. Outputs of the fitting algorithm: the first two plots are the measured and modeled power profiles, the third one is the difference between data and model weighted by their standard deviation, and the last one is the discrete gradient of T_e/T_i profile weighted by the regularization parameter.

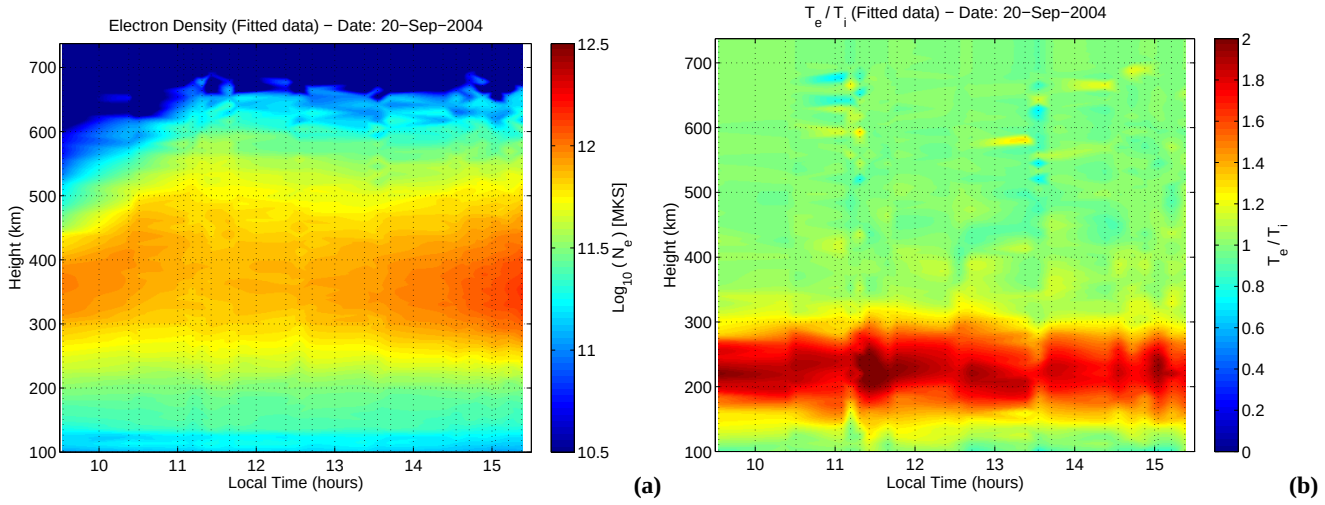

Fig. 8. (a) Electron density and **(b)** T_e/T_i estimates obtained on 20 September 2004.

with relatively low SNR, the inverted T_e/T_i values may be strongly biased. This fact motivated the inclusion of the regularization-term in the cost function (20) which is the discrete gradient of the temperature ratio profile weighted by λ. Our goal in applying regularization is to obtain smooth and unbiased T_e/T_i estimates.

The outcome of the inversion procedure has some dependence on the right choice of the regularization parameter. An optimal value of λ reduces the noise variance in the inversion results without biasing the model appreciably away from the measured data. Hansen (1992) describes a graphical method for choosing the regularization parameter which is named *L*-curve and consists in plotting the residuals of the data- and regularization-terms for different realizations of λ. The shape of this curve usually resembles an *L* and its "corner" or point of maximum curvature provides the optimal regularization parameter. The method is based on the criterion of equalizing the contributions of each term in the cost function (20).

Figure 6 displays one of the *L*-curves we computed for the data collected on 20 September 2004. In this case, a value of λ=1.58 provided the desired quality in our estimated profiles. Furthermore, we noticed that the *L* shape is not very sharp around the corner, and regularization parameters between 1 and 2 produced almost the same quality in the results. For other scans, we found optimal parameters within the same range, therefore, we chose a constant value of $\lambda = 1.5$ for all the estimations we performed.

In Fig. 7, we show some of the outputs of the fitting procedure corresponding to the same case of Fig. 6. The first two columns display the measured and modeled power profiles, the third one is the difference between data and model weighted by their uncertainties, and the last one is the regularization term. We are judging the quality of our fitting results following the *goodness-of-fit* criterion, which states that good estimates are obtained when the data-term normalized by the degrees of freedom of the data, i.e. the number of data points minus the number of estimating parameters, is around unity. Much larger or smaller values may imply a poor knowledge of σ_p and/or an inappropriate data model. In our estimations, we found values for the normalized data-term typically between 0.9 and 1.1, giving us confidence about the quality of our results.

5 Results and discussion

Figure 8 presents N_e and T_e/T_i maps for 20 September 2004, constructed from profile estimates obtained with the data model and inversion technique described in the previous sections. The density map shows a typical low-latitude F-region ionosphere exhibiting a characteristic rise during the morning hours. Also, T_e/T_i is elevated above unity mainly between 200 and 300 km as expected in daytime measurements.

In order to validate our results, we performed comparisons with electron density profiles obtained from the Roi-Namur digisonde system. As shown in Fig. 9, the agreement between fitted-ISR and digisonde estimates are excellent, specifically at the peak and bottom-side of the F-region. The agreement at the peak effectively verifies the correctness of the ALTAIR calibration constant K_s, whereas the agreement in the bottom-side verifies the forward model underlying the data inversion given that the values and altitudes of enhanced T_e/T_i are plausible in view of our understanding of the physics of the region. This was also verified by the good comparison of our results with temperature values obtained from the International Reference Ionosphere (IRI) model (e.g. Bilitza, 2001).

In Fig. 9, we are also comparing our fitted results with a set of power profiles from the vicinity of α=0°. They have

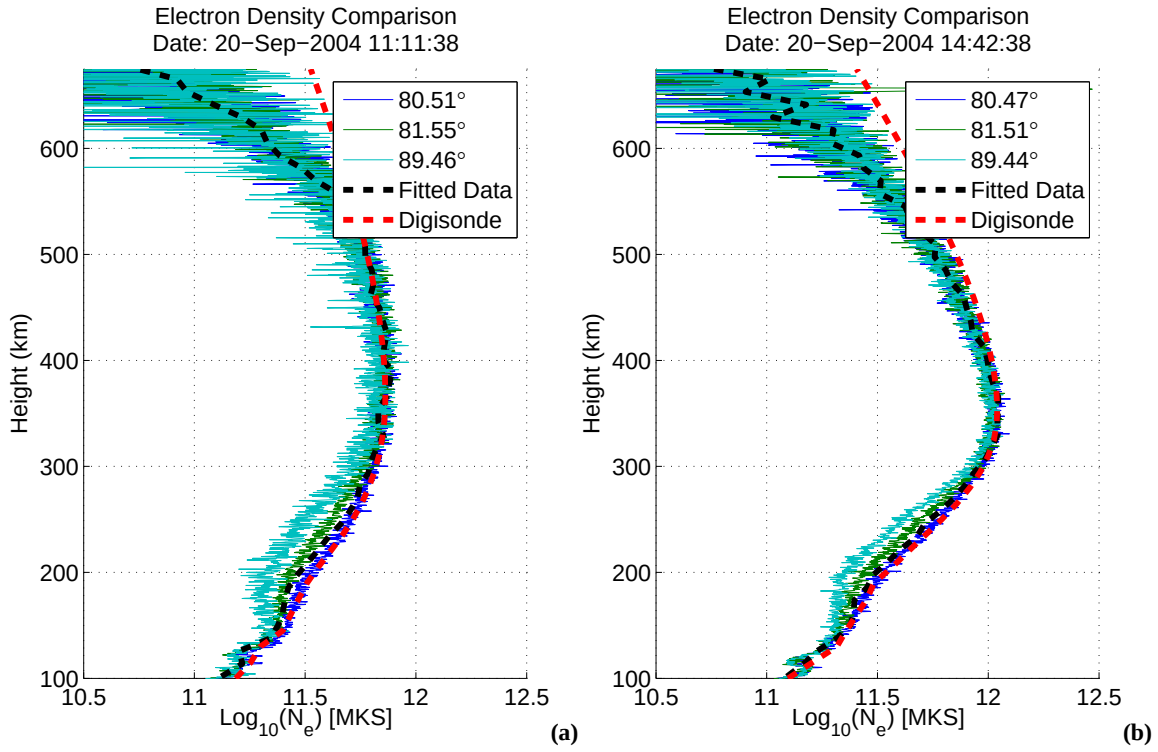

Fig. 9. Electron density comparison between fitted-ISR and digisonde measurements obtained **(a)** before and **(b)** after noon on 20 September 2004. We also display density-like profiles calculated by scaling the power data collected at directions around α=0° and assuming $\eta=\frac{1}{2}$ as if the ionosphere were in thermal equilibrium.

been scaled into equivalent density profiles by proper K_s and assuming $\eta=\frac{1}{2}$ as if the ionosphere were in thermal equilibrium. Somewhat surprisingly, we note that the profile corresponding to the scan angle closest to α=0° (about 80.5° elevation) agrees very well with the fitted-ISR and digisonde profiles. This may be the smooth result of having a moving beam with a finite width that averages the scattering contributions from different aspect angles around perpendicular to $\boldsymbol{B}$. Finally, note that the effect of $T_e/T_i>1$ disappears at altitudes below 130 km, where density estimates can be obtained at all elevation angles assuming $\eta=\frac{1}{2}$ as discussed in Kudeki et al. (2006) which is focused on E-region results of the same ALTAIR data set.

In summary, the technique described in this paper requires only a few scan directions across magnetic perpendicularity in order to obtain unbiased N_e and T_e/T_i estimates with a calibrated IS radar operating in the UHF band. The time resolution of the profile estimates can be improved by restricting the overall scan angle to a few degrees (2° or 3°) centered about α=0° and increasing the frequency of the scans. This procedure can also be applied with IS radars in VHF range provided that ionospheric depolarization effects, more important at VHF, are taken into account in a proper manner (e.g. Kudeki et al., 2003).

6 Conclusions

We have reported on N_e and T_e/T_i estimation with ALTAIR ISR power data at UHF obtained in meridional scans through the F-region ionosphere that included a radar probing direction orthogonal to the geomagnetic field. The estimation method makes use of a forward theory model of magnetic aspect angle as well as T_e/T_i dependence of the the total RCS of ionospheric incoherent scatter, including the proper physics of electron and ion Coulomb collisions formulated using a Fokker-Planck type collision model.

The physically meaningful results obtained in the experiment effectively verifies the forward theory model used in the inversion technique, including a new collision frequency dependent model for the total RCS of incoherent scattering at small aspect angles formulated in this paper. Indirectly, the electron collision frequency model proposed by Woodman (2004) has also been verified; however, the test of the frequency model was not very stringent given that the collision frequency dependence of the total RCS was found to be quite weak. Finally, we also regard the success of our data inversion procedure to be an indication that Woodman's collisional Gordeyev integral expressions, derived specifically for the $T_e=T_i$ case (Woodman, 1967), can also be used for $T_e>T_i$ as argued in Kudeki and Milla (2006).

Acknowledgements. We would like to thank the technical staff at the ALTAIR radar – in particular D. Sponseller, R. Ferguson, L. Schuett, J. Wathen, and P. Phu – for their cooperation and assistance during the NASA EQUIS 2 campaign. This work has been funded at the University of Illinois by NASA and NSF grants NAG5-5368 and ATM-0215246, respectively.

Topical Editor M. Pinnock thanks J. L. Chau and M. P. Sulzer for their help in evaluating this paper.

References

Bilitza, D.: International Reference Ionosphere 2000, Radio Science, 36, 261–275, 2001.

Dougherty, J. P. and Farley, D. T.: A theory of incoherent scattering of radio waves by a plasma, Proceedings of the Royal Society of London, Series A, Mathematical and Physical Sciences, 259, 79–99, 1960.

Farley, D. T.: A theory of incoherent scattering of radio waves by a plasma, 4. The effect of unequal ion and electron temperatures, J. Geophys. Res., 71, 4091–4098, 1966.

Farley, D. T., Dougherty, J. P., and Barron, D. W.: A theory of incoherent scattering of radio waves by a plasma, 2. Scattering in a magnetic field, Proceedings of the Royal Society of London, Series A, Mathematical and Physical Sciences, 263, 238–258, 1961.

Friedrich, M., Torkar, K. M., Lehmacher, G. A., Croskey, C. L., Mitchell, J. D., Kudeki, E., and Milla, M.: Rocket and incoherent scatter radar common-volume electron measurements of the equatorial lower ionosphere, Geophys. Res. Lett., 33, L08807, doi:10.1029/2005GL024622, 2006.

Hagfors, T. and Brockelman, R. A.: A theory of collision dominated electron density fluctuations in a plasma with applications to incoherent scattering, The Physics of Fluids, 14, 1143–1151, 1971.

Hansen, P. C.: Analysis of discrete ill-posed problems by means of the L-curve, SIAM Review, 34, 561–580, 1992.

Kudeki, E. and Milla, M.: Incoherent scatter spectrum theory for modes propagating perpendicular to the geomagnetic field, J. Geophys. Res., in press, 2006.

Kudeki, E., Bhattacharya, S., and Woodman, R. F.: A new approach in incoherent scatter F region $E \times B$ drift measurements at Jicamarca, J. Geophys. Res., 104, 28 145–28 162, 1999.

Kudeki, E., Woodman, R. F., and Feng, Z.: Incoherent scatter radar plasma density measurements at Jicamarca using a transverse-mode differential-phase method, Geophys. Res. Lett., 30(5), 1255, doi:10.1029/2002GL015496, 2003.

Kudeki, E., Milla, M., Friedrich, M., Lehmacher, G., and Sponseller, D.: ALTAIR incoherent scatter observations of the equatorial daytime ionosphere, Geophys. Res. Lett., 33, L08108, doi:10.1029/2005GL025180, 2006.

Lemnios, W. Z. and Grometstein, A. A.: Overview of the Lincoln laboratory ballistic missile defense program, Lincoln Laboratory Journal, 13, 9–32, 2002.

Levanon, N.: Radar principles, Wiley-Interscience publication, 1988.

Li, Y. L., Liu, C. H., and Franke, S. J.: Adaptive evaluation of the Sommerfeld-type integral using the Chirp z-Transform, IEEE transactions on antennas and propagation, 39, 1788–1791, 1991.

Sulzer, M. P. and González, S. A.: The effect of electron Coulomb collisions on the incoherent scatter spectrum in the F region at Jicamarca, J. Geophys. Res., 104, 22 535–22 551, 1999.

Tikhonov, A. N. and Arsenin, V. A.: Solutions of ill-posed problems, Winston & Sons, Washington, D.C., 1977.

Woodman, R. F.: Incoherent scattering of electromagnetic waves by a plasma, Ph.D. thesis, Harvard University, Cambridge, Massachusetts, 1967.

Woodman, R. F.: On a proper electron collision frequency for a Fokker-Planck collision model with Jicamarca applications, J. Atmos. S.-P., 66, 1521–1541, 2004.

Yeh, K. C., Chao, H. Y., and Lin, K. H.: A study of the generalized Faraday effect in several media, Radio Science, 34, 139–153, 1999.